Preliminary Result of Neoclassical Impurity Transport Affected by ICRH with a 4-D Fokker-Planck Code

Yunho Jeong [1], *Hyeonjun* Lee[1], *Nicola* Bertelli[2], *Eisung* Yoon[3], and *Jungpyo* Lee[1*]

[1]Hanyang University, Department of Nuclear Engineering, Seoul 04763, Republic of Korea
[2]Princeton Plasma Physics Laboratory, Princeton, NJ 08543, United States of America
[3]Ulsan National Institute of Science and Technology, Department of Nuclear Engineering, Ulsan 44919, Republic of Korea

Abstract. To understand the role of ion cyclotron resonance heating (ICRH) in mitigating tungsten accumulation, we evaluate the impact of ICRH-induced poloidal asymmetries on neoclassical impurity transport using a newly developed 4-D Fokker–Planck code (FP4D). Unlike conventional approaches that separate RF heating and transport modelling, FP4D solves both fast-ion distribution formation and impurity transport self-consistently without bounce-averaging. Benchmarking against the NEO code confirms the accuracy of the neoclassical physics in FP4D. Using FP4D, we analyze anisotropic and non-Maxwellian minority distributions under ICRH and their effects on the equilibrium potential and tungsten transport. Results show that anisotropy induced poloidal potential variations can reduce inward tungsten flux, depending on the modelling approach. Our findings highlight the importance of resolving the full velocity and poloidal structure of minority species in predicting impurity transport under strong RF heating conditions.

1 Introduction

Tungsten is a critical plasma-facing material in fusion devices, but its high-Z impurities tend to accumulate in the core and radiate power, degrading performance. Mitigation of tungsten accumulation by ICRH has been observed experimentally, and it is likely interpreted as resulting from two effects: (1) temperature screening [1], where increased logarithmic ion temperature gradient due to ICRH-heated ions reduce or even, under favorable conditions, reverse the inward impurity convection, and (2) poloidal asymmetry reduction, where ICRH-induced fast-ion temperature anisotropy alters the electrostatic potential on flux surfaces [2], redistributing W more uniformly [3]. In this work, we focus on investigating the second mechanism – the reduction of impurity poloidal asymmetry by ICRH – in order to better understand the role of RF-induced potential variations. Notably, such poloidal asymmetry reduction can manifest as a reduction of the inward neoclassical pinch [3].

Conventional modelling approaches have treated these effects in a two-step, uncoupled manner. Typically, a full-wave ICRH solver (such as TORIC [4]) coupled with a bounce-averaged Fokker-Planck solver (e.g., SSFPQL [5] or CQL3D [6]) is used to compute the fast-ion distribution for a minority heating species. This output (often assuming a bi-Maxwellian ion distribution with separate $T_\perp$ and $T_\parallel$) is used to evaluate the change in the lowest-order potential ($\tilde{\Phi}_0$) [3] which is then fed into a drift-kinetic neoclassical code (such as NEO [7,8]) to calculate impurity transport [9]. This approach is based on two assumptions as follows. First, the formation of fast ion distribution by ICRH on a long-time scale (i.e., the transport or ion collision time scale, second order in ρ_*) is independent of the neoclassical process that governs impurity transport on a shorter time scale (first order in ρ_*) to determine impurity transport. Second, the predetermined lowest-order potential is assumed to be sufficient to describe the effect of poloidal asymmetry, since the adiabatic response associated with a higher order potential ($\tilde{\Phi}_1$) does not contribute to the particle flux in the conventional neoclassical ordering.

In this study, we investigate the effect of the self-consistent poloidally varying potential ($\tilde{\Phi}_0 + \tilde{\Phi}_1$) by simultaneously solving the fast-ion distribution formation and the neoclassical drift-kinetic equation. The self-consistent potential can become important, when the ICRF power density is sufficiently strong and the poloidal inhomogeneity caused by the potential or wave absorption is non-negligible. In such cases, the first assumption becomes questionable, as the fast-ion distribution formation can be affected by the potential, which in turn modifies the neoclassical transport. In particular, this paper presents the effect of non-bounce averaged Fokker-Planck equation using the full fast-ion distribution, instead of a bi-Maxwellian distribution that assumes poloidally uniform adiabatic invariants.

For this work, we have developed a 4-dimensional Fokker-Planck code (FP4D), which is based on the global drift-kinetic equations [10] and solves the kinetic equations for the fast-ion distribution formation by RF

* Corresponding author: jungpyo@hanyang.ac.kr

heating and neoclassical transport within a single framework. FP4D does not assume a time-scale separation between RF application and transport response, and it does not perform bounce-averaging, instead resolving the full θ dependence of the distribution. By benchmarking FP4D against the NEO code for rotating plasmas and then applying it to ICRH-heated cases, we assess the impact of ICRH-induced anisotropy and non-Maxwellian effects on impurity transport. The goal is to provide more accurate and self-consistent predictions of tungsten behavior under ICRH, which is highly relevant for devising impurity control strategies in ITER and future reactors.

The paper proceeds as follows: Section 2 introduces the FP4D simulation framework. Section 3 investigates the mitigation of neoclassical impurity transport by ICRH, comparing conventional, non-Maxwellian, and self-consistent modelling approaches.

2 FP4D Code

2.1 FP4D code description

The FP4D code solves the drift-kinetic (Fokker-Planck) equation for each species' distribution function $f_a(r,\theta,v_\perp,v_\parallel,t)$ on an axisymmetric magnetic flux surface in 2D real space (radius r, poloidal angle θ) and 2D velocity space (perpendicular and parallel velocity $v_\perp, v_\parallel$). The code advances f_a according to a kinetic equation that includes parallel streaming, trapping and magnetic drift terms, full Coulomb collisions, external source and sink terms, and, importantly, an RF quasilinear operator for ICRH heating. A schematic form of the equation is:

$$\frac{\partial f_a}{\partial t} + (v_\parallel \mathbf{b} + \mathbf{v_{da}}) \cdot \nabla|_{\mu,W_a} f_a = C_a(f_a) + S_a(f_a) + S_{NB}(f_a) + Q_{RF}(f_a) + E_{DC}(f_a) - L_a(f_a), \quad (1)$$

where the left-hand side represents particle streaming along the field $v_\parallel \mathbf{b}\cdot\nabla|_{\mu,W_a} f_a$ and drift motions $\mathbf{v_{da}}\cdot\nabla|_{\mu,W_a} f_a$ (e.g. magnetic curvature and grad-B drift) in the tokamak, and the right-hand side includes collisions and RF wave effects. $C_a(f_a)$ denotes the Landau collision operator describing Coulomb collisions between species a and b [11], while $Q_{RF}(f_a)$ is the quasi-linear diffusion operator representing ICRH wave-particle interactions implemented in the Kennel–Engelmann form [12]. In this study, we focus on steady-state solutions ($\partial/\partial t = 0$) under a fixed RF power deposition.

FP4D is currently under development and verification. In the next section, we present a benchmarking against the NEO drift-kinetic code for neoclassical impurity transport. These benchmarks confirm that FP4D's physics modules (e.g., collisions, field solver) are verified prior to the ICRH application.

2.2 Benchmarking against NEO

Before examining ICRH effects, we verify that FP4D reproduces standard neoclassical results for impurity transport. We set up a JET-like case with parameters representative of a tokamak core plasma (at $r/a = 0.2$): deuterium as the main ion ($n_D = 5\times10^{19}$ m^{-3}), a trace tungsten impurity ($Z = 35$, $n_W = 10^{-5} n_D$), a hydrogen minority species ($n_H = 0.1 n_D$), and electrons ($n_e = \sum_i Z_i n_i$). In the absence of RF heating, all species are initialized with Maxwellian distributions ($T = 3$ keV) considering a toroidal rotation velocity $V_{tor} = 90$ km/s, which leads to a modest centrifugal force that can affect heavy impurity distribution (centrifugal enhancement of impurity concentration on the low-field side). We then compare particle fluxes computed by FP4D to those from the neoclassical code NEO. The benchmark results (Table 1) show good agreement within approximately 5 % of the relative error, except for the hydrogen minority, with small discrepancies that might result from numerical resolution. The cause of the deviation in the hydrogen minority is currently under investigation.

Table 1. Comparison of FP4D and NEO particle fluxes (m^{-2}s^{-1}) for a JET-like case ($r/a = 0.2$, without RF).

Particle Flux	e^-	D^+	W^{35+}	H^+
NEO	1.51E17	1.89E17	-7.21E14	-1.31E16
FP4D	1.53E17	1.99E17	-6.99E14	-2.18E16
Relative Error	1.05 %	5.04 %	-3.07 %	66.44 %

3 Neoclassical impurity transport mitigation due to ICRH

3.1 ICRH modelling

For the simulations, we adopt key parameters similar to the ICRF scenario described from [9], which has a 10% hydrogen minority in the deuterium plasma. The wave frequency is 42.5 MHz, which corresponding to the strong ICRF $n = 1$ fundamental cyclotron damping to hydrogen in the plasma core. The RF acceleration of minority ions is modeled with a perpendicular wavenumber $k_\perp = 50$ m^{-1}, parallel wave number $k_\parallel$ and frequency ω satisfying $(\omega - \Omega)/(k_\parallel v_{th}) = 1.0$ condition. For the impurity transport calculation in a flux surface at $r/a = 0.2$, the local RF power density is set to $P_{RF} = 0.5$ MW/m^3, providing a moderate level of ICRH heating to the minority species.

As shown in the FP4D simulation results in Fig. 1-(a), the hydrogen minority distribution function evolves into a strongly anisotropic steady state with $T_\perp > T_\parallel$ due to the perpendicular diffusion of cyclotron resonance. Starting from an isotropic Maxwellian at $T_0 = 3$ keV, the FP4D simulations predict a perpendicular temperature $T_\perp = 16.3$ keV and parallel temperature $T_\parallel = 7.6$ keV for the minority ions, yielding an effective temperature $T_{eff} = 13.4$ keV. For this result, constant Maxwellian background distributions were added for the main ions and electrons. Collisional energy transfer from the hydrogen minority to the background species leads to energy balance in the steady state. Consistent with this anisotropic heating, the minority density develops a pronounced poloidal variation as shown in

Fig. 1-(b), n_H is roughly proportional to $\cos\theta$, indicating a higher density on the outboard side of the flux surface, i.e., low-field side (LFS, at $\theta{\sim}0$) and lower density on the inboard side, i.e., high-field side (HFS). The $\cos\theta$ variation implies that more minority ions are trapped in banana orbits and localized on the LFS due to the anisotropy, since trapped particles spend more time near the outboard midplane.

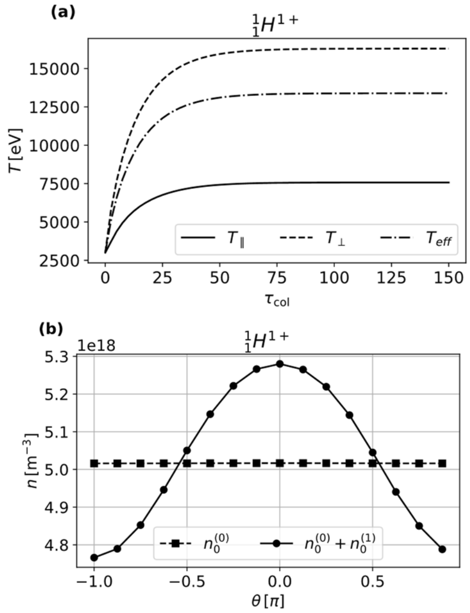

Fig. 1. ICRH minority heating results from FP4D. (a): Time evolution of the perpendicular and parallel temperature ($T_0 = 3$ keV) showing the anisotropy ($T_\perp > T_\parallel$). (b): Steady-state poloidal density profile of minority ions, exhibiting $\cos\theta$ variation peaked on the low-field side (LFS).

3.2 Conventional modelling

3.2.1 Approximation of anisotropic bi-Maxwellian

In order to evaluate the impact of the RF-driven minority anisotropy on heavy impurity transport, we first employ a conventional two-step, time-separated modelling approach. In this approach, the RF heating and the impurity transport are solved sequentially (in two separate FP4D simulations), under the assumption of decoupled time scales. Once the minority ion distribution is obtained from the first FP4D simulation, it is often approximated as a bi-Maxwellian form, which is described by two different temperatures ($T_\perp$ and $T_\parallel$). The distribution is given by

$$F_0 = \frac{n_0(\theta)(m/2\pi)^{3/2}}{T_\parallel^{1/2} T_\perp(\theta)} \exp\left(-\frac{mv_\parallel^2}{2T_\parallel} - \frac{mv_\perp^2}{2T_\perp(\theta)}\right), \quad (2)$$

where the perpendicular temperature $T_\perp(\theta)$ is poloidally varying. This form is based on the assumption of poloidally uniform invariants ($E = mv^2/2$ and $\mu = mv_\perp^2/2B$), which is consistent with the assumption of bounce-averaged Fokker-Planck equation. Based on this bi-Maxwellian distribution, the poloidal variation of density can be expressed as

$$n_{0a}(\theta) = n_{0a}(\theta_0)\frac{T_\perp(\theta)}{T_\perp(\theta_0)} \cdot$$

$$\exp\left[-\frac{Z_a e\tilde{\Phi}_0}{T_\parallel} + \frac{m_a\omega_0^2\{[R(\theta)]^2 - [R(\theta_0)]^2\}}{2T_\parallel}\right], \quad (3)$$

where the poloidal temperature, $T_\perp(\theta)$, is given by

$$\frac{T_\perp(\theta)}{T_\perp(\theta_0)} = \left[\frac{T_\perp(\theta_0)}{T_\parallel} + \left(1 - \frac{T_\perp(\theta_0)}{T_\parallel}\right)\frac{B(\theta_0)}{B(\theta)}\right]^{-1}. \quad (4)$$

As shown in Fig. 2-(a), the relative errors over the poloidal angle between the values obtained from Eq. (4) and the FP4D simulation results are approximately 1 % for $T_\perp$ and 5 % for $T_\parallel$, indicating that the bi-Maxwellian approximation with two anisotropic temperatures is reasonable.

For the FP4D simulation (with approximately $T_\perp = 16.3$ keV and $T_\parallel = 7.6$ keV for the minority H), the resulting lowest-order potential ($\tilde{\Phi}_0$) is solved under the quasi-neutrality condition ($\sum_a Z_a e n_{0a} = 0$), using the anisotropic density given in Eq. (3), which corresponds to the dashed line with squares in Fig. 2-(b). For comparison, the solid line with circles in Fig. 2-(b) represents a reference case in which the minority species is assumed to have an isotropic temperature ($T_\perp = T_\parallel = T_{eff} = 13.4$ keV). This isotropic case assumes uniform heating without introducing anisotropy and exhibits strong poloidal asymmetry due to the centrifugal force by toroidal rotation. In contrast, the anisotropic case exhibits additional $\cos\theta$ components in the potential profile, which arise from the temperature anisotropy shown in Fig. 2-(a). The increased population of hydrogen trapped particles on the low-field side generates the additional $\cos\theta$ component of the potential, which pushes the impurities as well as other ions toward the high-field side, as expected in [1].

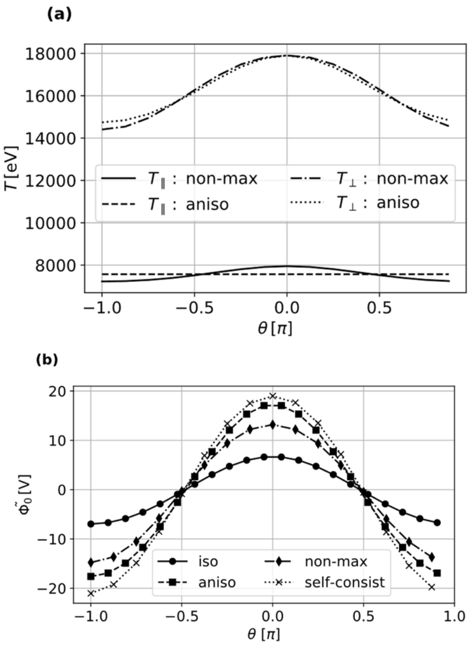

Fig. 2. (a): Comparison of the poloidal profiles of $T_\perp$ and $T_\parallel$ from FP4D simulation and the bi-Maxwellian approximation in Eq. (2). (b): Poloidal variation of the lowest-order potential $\tilde{\Phi}_0$ for cases with isotropic, anisotropic, non-Maxwellian, and self-consistent modelling. The corresponding $\cos\theta$ amplitudes are 6.62, 17.05, 13.2, and 18.99, respectively.

3.2.2 Effect of non-Maxwellian full distribution

However, the bi-Maxwellian distribution may lose the parallel physics that cannot be captured by the bounce-averaged equation. Fig. 3 shows the hydrogen distribution function in terms of the adiabatic invariants (or equivalently, velocity coordinates defined at the outer-midplane) for (a) poloidally uniform $m = 0$ mode and (b) $m = 1$ mode, obtained from the non-Maxwellian FP4D simulation results presented in Fig. 1 and 2. Under the poloidally uniform ICRF power absorption, the distribution function of $m = 1$ (non-adiabatic) is approximately 1% of the $m = 0$ mode. We find that the relative amplitude of the $m = 1$ mode becomes larger for the poloidally non-uniform ICRF power absorption, but the detailed analysis remains for future work. Interestingly, the non-adiabatic component could be important because the bounce-average does not eliminate potential variations acting on this portion of the distribution.

$$\int \frac{d\theta}{v_\parallel \mathbf{b}\cdot\boldsymbol{\nabla}\theta} v_\parallel \mathbf{b}\cdot\boldsymbol{\nabla}_{\mu,W_a=E+Z_a e\Phi} f = \int d\theta \left(-Z_a e \frac{\partial\Phi}{\partial\theta}\right)\frac{\partial f(E,\mu,\theta)}{\partial E}\ . \quad (5)$$

Specifically, Eq. (5) shows that the potential affects the non-adiabatic portion of the distribution even in the bounce-averaged formulation. Moreover, the quasilinear diffusion operator does not commute with bounce-averaging, i.e., $\langle Q_{RF}(f)\rangle_b \neq \langle Q_{RF}(F)\rangle_b$ which implies that the RF-induced change in hydrogen density cannot be fully captured by bounce-averaged models. Even for the $m = 0$ mode, non-Maxwellian features are evident from the difference between the dashed line with squares and the dash-dot line with diamonds in Fig. 2-(b).

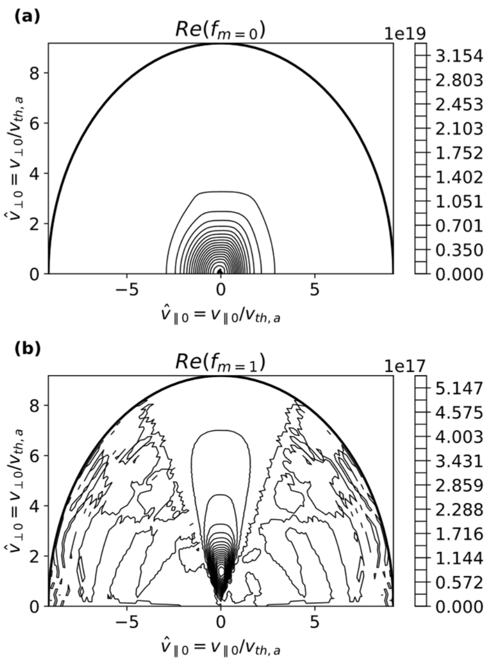

Fig. 3. FP4D hydrogen distribution function: (a) poloidally uniform $m = 0$ mode, (b) $m = 1$ mode showing non-adiabatic features not captured by bounce-averaged models.

3.2.3 Conventional modelling of neoclassical transport

After solving $\widetilde{\Phi}_0$ using the heated species density $n_H(\theta)$, this $\widetilde{\Phi}_0$ (which we might call a "$\widetilde{\Phi}_0$ correction" due to the RF heating) is used to compute the neoclassical transport for all species (in this case, electron, main deuterium ion, hydrogen as a heating species, and tungsten impurities). Table 2 summarizes the NEO and FP4D simulation results for the neoclassical transport.

Table 2. Core tungsten (W^{35+}) flux under various ICRH heating scenarios. Inward flux is reduced by ~ 34 % with anisotropic (d) and ~ 22 % with non-Maxwellian models (e), compared to the no-ICRH case (b). The fully self-consistent model shows the largest reduction (~ 63 %) (f).

Particle Flux	e^-	D^+	H^+	W^{35+}	
(a):Centrifugal Force X	1.49E17	1.69E17	-1.60E16	-8.91E13	
(b):Centrifugal Force O	1.51E17	1.89E17	-1.31E16	-7.21E14	Ref.
(c):ICRH + isotropic	1.60E19	1.19E17	6.50E16	-7.03E14	2.4 % ↓
(d):ICRH + anisotropic	1.63E17	1.60E17	2.03E16	-4.77E14	33.8 % ↓
(e):ICRH + non-Max	1.54E17	1.32E17	3.21E16	-5.60E14	22.3 % ↓
(f):ICRH + self-consist	1.49E17	8.39E17	-6.84E17	-2.67E14	63.1 % ↓

From cases (a) to (d) in Table 2, we use NEO to predict the tungsten impurity fluxes. The fluxes predicted by NEO differ markedly across these cases. The original case with rotation in (b) shows a significant increase of the inward tungsten flux compared to the original case without the rotation in (a). Adding the heating on hydrogen with the isotropic shows almost no change (2.4% reduction) in the tungsten flux, since the poloidally uniform temperature increase in the minority species does not modify the poloidal asymmetry, but only slightly alters the collisionality. As mentioned in the Introduction, the effect of the temperature gradient changes due to heating is beyond the scope of this study.

As shown in (d) of Table 2, introducing ICRH minority heating with anisotropic temperature tends to reduce the inward tungsten pinch compared to the isotropic temperature (c). The strong pressure anisotropy of the minority species modifies the equilibrium potential $\widetilde{\Phi}_0$ such that the original poloidal asymmetry of tungsten caused by the rotation is reduced, as shown in Fig. 4, thereby weakening the inward neoclassical convection. Fig. 4 shows the tungsten poloidal asymmetry for the isotropic Maxwellian (solid line with circles), the anisotropic Maxwellian (dashed line with squares), and the full non-Maxwellian distribution (dash-dot line with diamonds). In the anisotropic model, the steady-state inward tungsten flux is reduced by approximately 33.8% compared to the reference case. The non-Maxwellian case in Table 2-(e) and Fig. 4 (dash-dot line with diamonds) also predicts a reduction in the tungsten pinch, though to a lesser extent than the bi-Maxwellian case – approximately a 22.3% reduction in inward flux relative to the no ICRH. Notably, the tungsten flux predicted by the non-Maxwellian model lies between the isotropic and anisotropic Maxwellian cases. This suggests that the simple bi-Maxwellian representation may somewhat overestimate the beneficial effect of ICRH in reducing tungsten accumulation. In other words, accurately capturing the detailed velocity-space structure of the minority distribution is crucial for quantifying impurity transport effects.

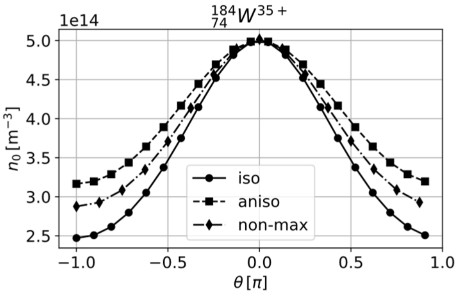

Fig. 4. Poloidal asymmetry of tungsten density for cases with isotropic, anisotropic and non-Maxwellian hydrogen distributions.

3.3 Self-consistent modelling with FP4D

To assess the effect of the self-consistent potential, the evolution of the heating species distribution and the impurity transport are solved simultaneously in FP4D, in the presence of the poloidally varying potential, which is self-consistently calculated by the quasi-neutrality conditions. Importantly, we retain full poloidal resolution of the distribution functions – no bounce averaging is applied – so poloidal asymmetries in density and potential naturally arise and feedback into the transport. As shown in the last term on the right-hand side of Eq. (6), the correction to the parallel dynamics due to the full potential ($\widetilde{\Phi} = \widetilde{\Phi}_0 + \widetilde{\Phi}_1$) is included, without differentiating the order of $\widetilde{\Phi}_0$ and $\widetilde{\Phi}_1$. This self-consistent FP4D modelling allows the minority distribution, the impurity distribution, and the electric fields ($\widetilde{\Phi}_0$ and $\widetilde{\Phi}_1$) to evolve together until a steady state consistent with all physical effects is reached.

$$v_\parallel \mathbf{b}\cdot\nabla|_{\mu,W_a=E+Z_a e\Phi} f_a = (v_\parallel \mathbf{b}\cdot\nabla\theta)\cdot \left[\frac{\partial f_a}{\partial\theta} + \frac{v_\perp}{2Bv_\parallel}\frac{\partial B}{\partial\theta}\left(v_\parallel\frac{\partial f_a}{\partial v_\perp} - v_\perp\frac{\partial f_a}{\partial v_\parallel}\right) - \frac{Z_a e}{m_a}\frac{\partial\Phi}{\partial\theta}\frac{1}{v_\parallel}\frac{\partial f_a}{\partial v_\parallel}\right]. \qquad (6)$$

When we enable the full physics, we observe a further reduction in the tungsten inward flux. In the fully self-consistent case, as shown in Table 2-(f), the steady-state tungsten W^{35+} flux into the core is 63.1% lower than in the isotropic no-RF case. Further analysis and verification of the self-consistent results remains as future work.

4 Conclusion

In this study, we evaluated the effect of ICRH-induced poloidal asymmetries on neoclassical impurity transport using a newly developed 4-D Fokker–Planck code (FP4D). By avoiding bounce-averaging and solving the fast-ion distribution and impurity transport self-consistently, FP4D provides a more complete description of the physical processes involved. Benchmarking against the NEO code confirms the validity of the neoclassical physics implemented in FP4D. Our results show that anisotropy and non-Maxwellian features in the heated minority distribution significantly modify the equilibrium potential and reduce inward tungsten flux. Moreover, a fully self-consistent treatment that evolves both the minority and impurity distributions under the same potential yields the largest reduction in tungsten accumulation. This mitigation does not indicate a reversal to outward impurity flux, but rather a reduction of the inward neoclassical pinch. These findings underscore the importance of resolving the full velocity-space structure and poloidal variations of heated species in impurity transport modelling under strong RF heating.

This research was supported by Korean Institute for Advancement of Technology (KIAT) grant funded by the Korea Government (MOTIE) (RS-2024-00435157, Human Resource Development Program for Industrial Innovation (Global))

References

1. C. Angioni, P. Helander, Neoclassical transport of heavy impurities with poloidally asymmetric density distribution in tokamaks, Plasma Phys. Control. Fusion **56**, 124001 (2014). https://doi.org/10.1088/0741-3335/56/12/124001
2. W. Choe, C.S. Chang, M. Ono, Temperature anisotropy in a cyclotron resonance heated tokamak plasma and the generation of poloidal electric field, Phys. Plasmas **2**, 2044 (1995). https://doi.org/10.1063/1.871456
3. R. Bilato, O. Maj, C. Angioni, Modelling the influence of temperature anisotropies on poloidal asymmetries of density in the core of rotating plasmas, Nucl. Fusion **54**, 072003 (2014). https://doi.org/10.1088/0029-5515/54/7/072003
4. M. Brambilla, Numerical simulation of ion cyclotron waves in tokamak plasmas, Plasma Phys. Control. Fusion **41**, 1 (1999). https://doi.org/10.1088/0741-3335/41/1/002
5. M. Brambilla, Quasi-linear ion distribution function during ion cyclotron heating in tokamaks, Nucl. Fusion **34**, 1121 (1994). https://doi.org/10.1088/0029-5515/34/8/I06
6. R.W. Harvey, M.G. McCoy, The CQL3D Code, IAEA TCM on Advances in Simulation and Modeling of Thermonuclear Plasmas, USDOC/NTIS, Paper No. DE93002962, 489–526 (1992)
7. E.A. Belli, J. Candy, Kinetic calculation of neoclassical transport including self-consistent electron and impurity dynamics, Plasma Phys. Control. Fusion **50**, 095010 (2008). https://doi.org/10.1088/0741-3335/50/9/095010
8. E.A. Belli, J. Candy, Full linearized Fokker–Planck collisions in neoclassical transport simulations, Plasma Phys. Control. Fusion **54**, 015015 (2011). https://doi.org/10.1088/0741-3335/54/1/015015

9. F.J. Casson, C. Angioni, E.A. Belli, R. Bilato, P. Mantica, T. Odstrcil, et al., Theoretical description of heavy impurity transport and its application to the modelling of tungsten in JET and ASDEX Upgrade, Plasma Phys. Control. Fusion **57**, 014031 (2014). https://doi.org/10.1088/0741-3335/57/1/014031
10. M. Landreman, F.I. Parra, P.J. Catto, D.R. Ernst, I. Pusztai, Radially global δf computation of neoclassical phenomena in a tokamak pedestal, Plasma Phys. Control. Fusion **56**, 045005 (2014). https://doi.org/10.1088/0741-3335/56/4/045005
11. E.S. Yoon, C.S. Chang, A Fokker-Planck-Landau collision equation solver on two-dimensional velocity grid and its application to particle-in-cell simulation, Phys. Plasmas **21**, 032503 (2014). https://doi.org/10.1063/1.4867359
12. C.F. Kennel, F. Engelmann, Velocity space diffusion from weak plasma turbulence in a magnetic field, Phys. Fluids **9**, 2377 (1966). https://doi.org/10.1063/1.1761629